PHYSICAL REVIEW B **93**, 045404 (2016)

Disorder-assisted transmission due to charge puddles in monolayer graphene: Transmission enhancement and local currents

Leandro R. F. Lima[*] and Caio H. Lewenkopf
Instituto de Física, Universidade Federal Fluminense, 24210-346 Niterói, Brazil

(Received 16 October 2015; published 6 January 2016)

We investigate the contribution of charge puddles to the nonvanishing conductivity minimum in disordered graphene flakes at the charge neutrality point. For that purpose, we study systems with a geometry that suppresses the transmission due to evanescent modes allowing us to single out the effect of charge fluctuations in the transport properties. We use the recursive Green's function technique to obtain local and total transmissions through systems that mimic vanishing density of states at the charge neutrality point in the presence of a local disordered local potential to model the charge puddles. Our microscopic model includes electron-electron interactions via a spin resolved Hubbard mean field term. We establish the relationship between the charge puddle disorder potential and the electronic transmission at the charge neutrality point. We find that electronic interactions do not play a significant role in this setting. We discuss the implications of our findings to high mobility graphene samples deposited on different substrates and provide a qualitative interpretation of recent experimental results.

DOI: 10.1103/PhysRevB.93.045404

I. INTRODUCTION

The peculiar electronic transport properties of graphene have triggered numerous experimental and theoretical studies [1–3]. Of particular interest is the conductivity of graphene single layers at the charge neutrality point (CNP). Experiments [4,5] have confirmed the theoretical prediction [6] that the conductivity minimum is $4e^2/\pi h$ for short and wide undoped ballistic samples. For larger high mobility graphene flakes deposited on oxide substrates [7,8], the conductivity shows a minimum close to $4e^2/h$. This enhancement is in line with theoretical works that show that disorder increases the graphene conductivity at the CNP [9–12]. This counterintuitive result is interpreted as a manifestation of Klein tunneling [13,14] and weak antilocalization [15]. Inhomogeneous electron-hole charge puddles [16,17] are believed to be the main source of disorder in undoped graphene systems [1,18,19].

Charge puddles are ubiquitous in single-layer graphene samples deposited on a substrate [16,17,20], but their origin is still under debate [21–25]. Charge inhomogeneities can be formed, for instance, by charges trapped in the substrate [16,26]. Some authors argue that ripples can induce charge puddles [24,25], but typical experimental data show only a weak spacial correlation between the latter [23,24]. It should be mentioned that at high doping, transport measurements of graphene on substrates with very different dielectric constants [21,22] show surprisingly similar sample mobilities, indicating that charge distribution fluctuations are unlikely to be the dominant source for electron momentum relaxation processes away from the CNP.

Scanning tunneling microscopy (STM) studies [20,27] of the local chemical potential μ_{loc} at charge neutrality provide further insight. They reveal that the charge fluctuations in graphene monolayers on hexagonal boron nitride (hBN) [27] are about an order of magnitude smaller than those on silicon dioxide ($\mathrm{SiO_2}$) samples [20]. In both cases the data show that μ_{loc} follows a Gaussian distribution with a standard deviation of 5.4 ± 0.1 meV for hBN and 55.6 ± 0.7 meV for $\mathrm{SiO_2}$. Some authors find a typical charge puddle size $a \approx 20$ nm [28] independent of the substrate, while others [20] show that the puddles in graphene on $\mathrm{SiO_2}$ are smaller than those of graphene on hBN.

Several theoretical studies investigate the effect of a local long range or chemical potential disorder at the charge neutrality point [2,9,11,12,29]. In terms of the ratio between the electron elastic mean free path ℓ and the system size L, the following picture emerges: While for $\ell/L > 1$ the transport is ballistic and dominated by evanescent modes [6], deep in the diffusive regime $\ell/L \ll 1$, the conductivity is governed and enhanced by potential fluctuations scattering that lead to weak antilocalization [2].

Recent experimental studies report an insulator behavior in single-layer graphene on boron nitrite at the neutrality point [30,31]. Reference [31] shows that the conductivity minimum depends strongly on the matching between the graphene and the hBN lattice constants. Reference [30] observes a resistivity as high as several megaohms per square for low temperatures, $T \approx 20$ mK, with a power law increase with temperature. A metal-insulator transition driven by decreasing rather than by increasing the charge puddle disorder has also been reported in graphene double layers [32]. These observations do not fit in the general picture and call for further investigation.

In summary, although it is widely accepted that disordered charge puddles are responsible for an enhancement of the conductivity minimum at the CNP, there is very little quantitative support for this picture, particularly at the ballistic-diffusive crossover regime. On one hand, analytical works rely on semiclassical arguments that require charge puddles with a large number of electrons [3,18], a condition hardly met by experiments. On the other hand, numerical simulations typically contain contributions of evanescent modes [6] that are inextricably mixed with those due to charge inhomogeneities, obscuring the latter. The main goal of this paper is to disentangle these contributions and to single out the effects of charge puddles in the conductivity of disordered graphene sheets close to the neutrality point.

---

[*] Corresponding author: leandrolima@if.uff.br

For that purpose, we analyze the transport properties of graphene systems with geometries that quench evanescent modes using a self-consistent recursive Green's function (RGF) technique [33,34] with spin resolution that includes the electronic interaction via a mean field Hubbard term. We calculate electronic current densities between neighboring carbon sites. We analyze the electronic propagation near *pn* charge puddle interfaces, relating the general transport properties to the typical puddles characteristics, such as their charge, size, and shape.

This paper is organized as follows. In Sec. II we present the model Hamiltonian we employ to describe graphene sheets with disordered charge puddles. There we also discuss the key ingredients necessary to calculate transport properties and to realistically assess the minimum conductivity at the CNP using a lattice model of a moderate size. In Sec. III we present the total and local transmissions for different potential profiles, establishing a qualitative understanding of the role of charge puddles in the electronic transport. We present our conclusions in Sec. IV.

II. MODEL AND THEORY

We model the electronic properties of a monolayer graphene sheet by a Hubbard mean field π-orbital tight-binding model, namely [1,33,35]

$$H = -t \sum_{\langle i,j\rangle,\sigma} a_{i,\sigma}^{\dagger} a_{j,\sigma} + \sum_{i,\sigma} U\left(\langle \hat{n}_{i,-\sigma}\rangle - \frac{1}{2}\right)\hat{n}_{i,\sigma} + \sum_{i,\sigma} V_i\, \hat{n}_{i,\sigma}, \quad (1)$$

where $a_{i,\sigma}^{\dagger}$ ($a_{i,\sigma}$) stands for the operator that creates (annihilates) an electron with spin σ at the site i, $\hat{n}_{i,\sigma}$ is the corresponding electron number operator, while $\langle \hat{n}_{i,\sigma}\rangle$ is its expectation value, t is the hopping matrix element connecting states at neighboring sites, and $\langle i,j\rangle$ indicates that the sums are restricted to first neighbor sites. The electron-electron interaction is approximated by the Hubbard mean field term, where U is the Coulomb energy for double occupancy of a carbon site [33]. The choice of this effective interaction is justified by the remarkable agreement between the Hubbard mean field and density functional calculations of the electronic properties of graphene nanoribbons [36].

We assume that the electron-hole puddles are generated by a disordered long-range local potential $V(\mathbf{r})$. We model $V(\mathbf{r})$ in the lattice, $V_i = V(\mathbf{r}_i)$, by a superposition of N_G Gaussian potentials centered at the positions $\mathbf{r}_p = (x_p, y_p)$, namely

$$V_i = \sum_{p=1}^{N_G} V_p \exp\left[-2\frac{(x_i - x_p)^2}{d_x^2} - 2\frac{(y_i - y_p)^2}{d_y^2}\right]. \quad (2)$$

We consider V_p to be either V or $-V$ with equal probability, and the positions $\mathbf{r}_i$ are random and uniformly distributed over the graphene flake. Suitable choices of the Gaussian range parameters d_x and d_y allow us to study different physical regimes, as discussed in the next section. For $d_x = d_y$ this model is equivalent to a Gaussian disordered model studied by several authors [9,11,29].

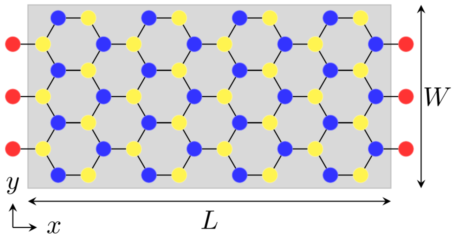

FIG. 1. Sketch of an armchair GNR of length L and width W. The red sites represent semi-infinite linear chains connected to source or drain reservoirs.

A. Model geometry

Our main goal is the study of the effect of charge puddles in transport properties in graphene flakes near the charge neutrality point. From the perspective of simulations, the difficulty is that the current numerical methods based on microscopic models that take into account interactions or address local transport properties are computationally prohibitive for systems of realistic sizes. For that reason we study much smaller systems, with similar properties of bulk graphene, and resort to a scaling scheme to draw conclusions. In what follows we show that this is accomplished by using armchair graphene nanoribbons (GNRs), such as the one depicted in Fig. 1.

In the absence of electron-electron interaction, GNRs with zigzag edges are always metallic. Armchair GNRs are metallic when the number of hexagons across the transverse direction is $M = 3i$, where i is an integer number, and semiconductor otherwise [37]. Both zigzag and armchair metallic GNRs show a unit transmission per spin channel as the doping goes to zero. This metallic behavior, related to boundary effects, is unlikely to be manifest in the bulk and makes it difficult to single out the effects of charge puddles in the conductance. Electronic interactions give rise to a gap in zigzag and chiral GNRs with pristine edges, which is a condition hardly met by graphene flakes. Thus, we find it more convenient to use semiconductor armchair GNRs for this study.

It is convenient to express the length L and the width W of armchair GNRs as $L = N(\sqrt{3}a_0/4)$ and $W = Ma_0$, where N gives the number of sites in an armchair chain along the GNR length and M is the number of hexagons across its width. $a_0 = 2.46$ Å is the lattice parameter. The total number of sites in the system is $N_{\rm tot} = (2M + 1)N/2$. Figure 1 illustrates an armchair GNR with $M = 3$, $N = 16$, and $N_{\rm tot} = 56$.

The energy threshold E_1 to open the first propagating channel depends on the nanoribbon width W (or equivalently on M) roughly as the inverse width [38]. The W^{-1} threshold behavior we infer for interacting pristine graphene ribbons was theoretically predicted for noninteracting nanoribbons [37] and observed in experiments [39]. In the latter case, the systems are more complex and the threshold behavior is understood in terms of edge disorder [40]. With increasing W, the system properties become increasingly similar to bulk graphene: The bands collapse into a conical one and the energy gap goes to zero, resulting in a vanishing DOS at the charge neutrality point.

B. Transport calculations

We obtain the system transport properties using the nonequilibrium Green's function technique [41,42]. We calculate the system Green's functions using the mean field Hamiltonian given by Eq. (1) for the two-contact lattice geometries shown in Fig. 1. For that purpose, we use the recursive Green's function method [34] combined with a self-consistent procedure [33] that we describe below.

We compute the conductance using the partition geometry shown in Fig. 1. The semi-infinite chains placed at the right (R) and the left (L) side of the central region represent the leads that connect the graphene flake to source and drain reservoirs. The system Hamiltonian, Eq. (1), the Green's functions, and the transport properties depend self-consistently on the system electronic density $\langle \hat{\mathbf{n}} \rangle$.

In the zero bias limit, the self-consistent relationship that connects the electronic density and the system retarded Green's function $\mathbf{G}^r$ reads [42]

$$\langle \hat{n}_{i,\sigma}(\mu) \rangle = - \int_{-\infty}^{\infty} \frac{dE'}{\pi} f(E') \,\mathrm{Im}\left[G^{r,\sigma\sigma}_{i,i}(E')\right], \qquad (3)$$

where $f(E)$ is the Fermi-Dirac distribution at the source and drain reservoirs with corresponding chemical potentials $\mu_\mathrm{L} \approx \mu_\mathrm{R} \approx \mu$. For the systems of interest, where $N_\mathrm{tot} \gg 1$, $\mathbf{G}^r(E)$ has a large number of complex poles and shows fast energy variations close to charge neutrality. Thus, a real-axis numerical evaluation of the integral in Eq. (3) is very costly, since good accuracy demands a fine integration mesh.

Efficient methods [43–45] developed to evaluate the integral in Eq. (3) use complex analysis, taking advantage of the analytical structure of $\mathbf{G}^r(E)$. Since the poles ε_p of the retarded Green's function lie in the lower complex half-plane, $\mathrm{Im}(\varepsilon_p) < 0$, Eq. (3) is readily evaluated by a contour integration. The integration limits have to be treated carefully: To guarantee charge conservation all states must be inside the integration limits [45]. The Fermi function provides an effective upper energy cutoff but introduces Matsubara poles in the upper complex half-plane. To efficiently deal with these issues, we use the integration technique described by Ozaki in Ref. [43]. The method expands the Fermi-Dirac distribution in a partial fraction decomposition, so that the integral in Eq. (3) is given by a sum of $N_{\bar{E}}$ evaluations of $\mathbf{G}^r(\bar{E}_j)$ at the complex energies $\bar{E}_j$, with $j = 1,\dots,N_{\bar{E}}$ [43].

Two key features of this method are noteworthy: (i) There is no need to specify the lower energy bound and (ii) the integration precision is controlled by varying $N_{\bar{E}}$. To attain a given accuracy, smaller temperatures require larger $N_{\bar{E}}$ values. We choose $kT = 25$ meV. This temperature is very amenable for the numerical calculation and, since $kT/E_1 < 1$, it still guarantees that we address a low temperature regime for the systems we study. We find that $N_{\bar{E}} \approx 40$–50 guarantees an error smaller than 10^{-5} for the electronic densities we study in this paper. For the systems we analyze, this method is three orders of magnitude faster than a real-axis integration. Nonetheless, the calculation of $\langle \hat{\mathbf{n}} \rangle$ still remains as the computational bottleneck that limits the conductance evaluation of large model systems.

The self-consistent procedure we employ is rather standard: We start with an initial guess for $\langle \hat{\mathbf{n}}_\mathrm{in}(\mu) \rangle$, obtain the system retarded Green's function $\mathbf{G}^r(E)$ using the RGF method [34], and calculate the updated equilibrium electronic density $\langle \hat{\mathbf{n}}_\mathrm{out}(\mu) \rangle$ using Eq. (3). For the subsequent iterations we use the modified second Broyden method [45–47] that mixes all the previous input and output electronic densities to construct an optimized input $\langle \hat{\mathbf{n}}_\mathrm{in}(\mu) \rangle$ for the next self-consistent iteration. The procedure is repeated until convergence is achieved. Our convergence criteria is $|\langle \hat{\mathbf{n}}_\mathrm{in}(\mu) \rangle - \langle \hat{\mathbf{n}}_\mathrm{out}(\mu) \rangle| < 10^{-5}$, for which the required number of iterations is 20 up to $\sim$40 depending on system size. For the systems we study, self-consistent loop procedures that naively update $\langle \hat{\mathbf{n}}_\mathrm{in}(\mu) \rangle$ with the occupations obtained from the previous iteration, $\langle \hat{\mathbf{n}}_\mathrm{out}(\mu) \rangle$, are about 10^2 times slower than those that use the Broyden method [48].

Once convergence is achieved, we calculate the transport quantities, such as the total transmission coefficient between L and R contacts [41]

$$T^{\sigma}_{\mathrm{L,R}}(E) = \mathrm{Tr}\left[\Gamma^{\sigma}_{\mathrm{L}}(E)\mathbf{G}^{r,\sigma\sigma}(E)\Gamma^{\sigma}_{\mathrm{R}}(E)\mathbf{G}^{a,\sigma\sigma}(E)\right] \qquad (4)$$

and the local transmission coefficient between the neighboring i and j sites [34,49–52]

$$T^{\sigma}_{i,j}(E) = -2t\,\mathrm{Im}\left\{\left[\mathbf{G}^{r,\sigma\sigma}(E)\Gamma^{\sigma}_{\mathrm{L}}(E)\mathbf{G}^{a,\sigma\sigma}(E)\right]_{i,j}\right\}. \qquad (5)$$

The advanced Green's function is obtained from $\mathbf{G}^{a,\sigma'\sigma}(E) = [\mathbf{G}^{r,\sigma\sigma'}(E)]^\dagger$. The linewidth functions are $\Gamma^{\sigma}_{\alpha}(E) = -2\,\mathrm{Im}\,\Sigma^{r,\sigma}_{\alpha}(E)$. Here $\Sigma^{r,\sigma}_{\alpha}$ is the retarded self-energy associated with the decay into $\alpha = \mathrm{L}$ and R leads and is calculated following a standard procedure [34].

Equations (4) and (5) assume the injection of electrons is spin independent, $\Gamma^{\sigma}_{\alpha} = \Gamma^{\bar{\sigma}}_{\alpha}$, and the absence of spin-flip processes. Thus, at sufficiently low temperatures, the zero bias limit conductance of the system for an electronic energy E is $G(E) = 2(e^2/h)T_{\mathrm{L,R}}(E)$, where $T_{\mathrm{L,R}} \equiv T^{\sigma}_{\mathrm{L,R}} = T^{\bar{\sigma}}_{\mathrm{L,R}}$. In the diffusive regime, the conductance G can be converted into a conductivity σ using $\sigma = (L/W)G$.

In the absence of electron-electron interactions, the aspect ratio L/W dictates the conductance of pristine graphene sheets [6]. For $W/L \gg 1$, evanescent modes lead to a conductivity minimum of the order e^2/h at the charge neutrality point, both for semiconductor and metallic graphene ribbons [6]. In the opposite limit of narrow and/or long ribbons, $W/L \ll 1$, the conductivity goes to zero.

We find that, for ballistic graphene systems, electron-electron interactions do not qualitatively change this picture. This statement is based on the study of the transmission through pristine semiconductor graphene flakes with armchair edges connected to generic metallic leads. We consider different sizes and aspect ratios using $U = t$ [53]. Our results are summarized in Fig. 2.

As in the noninteracting case, the transmission dependence on the geometry can be cast in terms of the aspect ratio. We compute $T(E_F)$ for $L/W = 1$, 2, and 5. Since we work in the low temperature regime, we define $E_F = \mu$. For each value of L/W we consider different system sizes defined by M. Recall that $W = Ma_0$. Figure 2 shows that by expressing the electronic energy as $\varepsilon = E_F/E_1$, all $T(E_F)$ corresponding to GNRs with the same aspect ratio L/W collapse into a single curve. For $L/W = 1$, the transmission minimum at $E_F = 0$ is roughly $T \approx 0.44$. Electron-electron interaction effects in the

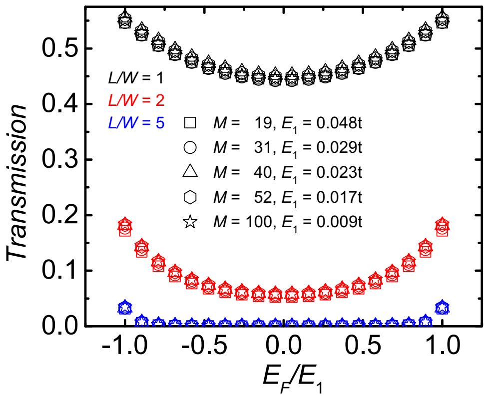

FIG. 2. Total transmission T of armchair GNRs of different widths W connected to generic metallic leads as a function of the ratio between the energy E_F and the first threshold energy of the first conducting channel $E_1(W)$. The behavior of T versus E_F/E_1 depends only on the GNR aspect ratio L/W.

mean field approximation only strongly affect the transmission for states with a high density of states at the edges of zigzag GNRs [36,54], which is not the case for armchair GNRs; the noninteracting value of the transmission minimum is roughly the same as that for $U = 0$.

The noninteracting result $T(0) = 2/\pi \approx 0.64$ found analytically in Ref. [6] and reproduced numerically in Ref. [34] differs from our calculation due to the different modeling of the leads. While we use linear chain as contacts, these previous works used square lattices that provide additional nondiagonal self-energy elements, changing the leaking probability of the electrons. For $L/W = 2$, the transmission minimum decreases to about 0.05. Finally, zero transmission is obtained if the ratio is as large as $L/W = 5$.

These results show that the evanescent modes contribution indeed depends only on the aspect ratio L/W and that their contribution to the conductance is almost entirely suppressed for $L/W > 5$. As a consequence, even a 5-μm-long semiconductor graphene flake may have a nonvanishing transmission minimum at $E_F = 0$ due to evanescent modes if $W > 1$ μm. In the remainder of this paper we eliminate the effect of evanescent modes by considering graphene systems with $L/W \geqslant 5$.

III. RESULTS

In this section we study the effects of charge puddles on the transmission minimum close to the charge neutrality point by considering different models for $V(\mathbf{r})$. To develop some insight into the role of interactions and the variations on the local potential, we begin discussing the simple case of a *pn* junction before we proceed to cases of disordered charge puddles.

A. *pn* junctions: $U = 0$ limit case

We model the *pn*-junction interface potential $V(\mathbf{r})$ by taking $d_y \gg W$ in Eq. (2) that corresponds to a constant potential along the GNR width. We consider a system with $M = 52$ and choose the smallest value of N that gives an aspect ratio $L/W \geqslant 5$, namely $N = 604$. We generate a *pn* junction by placing a positive Gaussian potential centered at the site $(L/4, W/2)$ and a negative one at $(3L/4, W/2)$. We choose $d_x = 0.24L$. At the p- and n-doped regions, the local potential is constant and set to $V(\mathbf{r}) = V$ for $0 \leqslant x \leqslant L/4$ and $V(\mathbf{r}) = -V$ for $3L/4 \leqslant x \leqslant L$. This choice renders a $V(\mathbf{r})$ with a smooth Gaussian transition between positively and negatively doped regions.

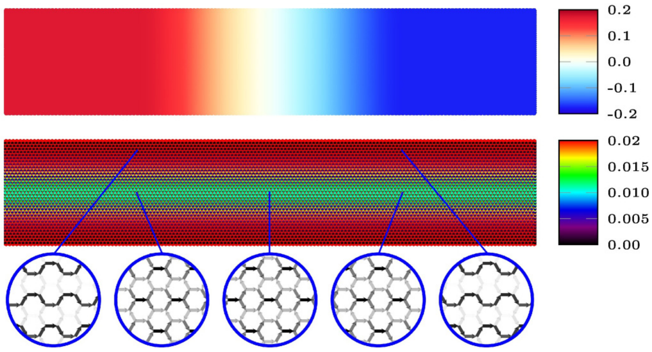

FIG. 3. Top: Potential profile of a smooth *pn* junction for $M = 52$. The energy scale on the right is given in units of t. Middle: Corresponding profile of the local transmission at $E_F \approx 0.15E_1$. Bottom: Zoom of the local transmission at selected areas.

We obtain E_1 by inspecting the corresponding dispersion relation. We choose the potential strength $V = 10E_1$. The top panel of Fig. 3 shows the contour plot of the *pn*-junction potential $V(\mathbf{r})$, while Fig. 5 shows $V(\mathbf{r})$ along the system longitudinal direction.

We compute the local transmissions for selected energies close to the charge neutrality point using Eq. (5). We recall that in this subsection we set $U = 0$. The middle panel of Fig. 3 shows the local current density profile at the energy $E_F = 0.15E_1$. This energy lies inside the transport gap of the GNR in the absence of the *pn* junction, that is for $V = 0$. The current near the system edges is mainly transmitted through "armchair chains" (see insets at the bottom of Fig. 3), similar to the transmission through pristine armchair GNRs. At the center of the ribbon, backscattering processes mix the transmission between different armchair chains generating a richer transmission structure. The local transmission profile is almost invariant along the system longitudinal direction, including the p- and n-doped regions and their interface.

Figure 4 shows the total transmission $T(E_F)$ as a function of the electronic energy E_F for several values of V. The main features are: (i) $T(E_F)$ shows Fabry-Perot interference oscillations caused by backscattering at the abrupt potential interfaces between the graphene central region and the right and left contacts. (ii) The transport gap, centered at $E_F = 0$ for $V = 0$, appears twice at $E_F + V$ and at $E_F - V$. (iii) Around the CNP, between the two gapped regions, where otherwise one would expect a transport gap, the transmission increases with V. (iv) For large values of V (see, for instance, $V/E_1 \gtrsim 7$), the transmission near the CNP shows E_F dependent fluctuations, but $T(E_F)$ remains between 0.5 and 1.

In Fig. 5 we present a sketch that suggests a simple explanation of the main features of the transmission through the smooth *pn* junction in terms of the local band structure. For $0 < x < L/4$, the potential $V(\mathbf{r}) = V$ shifts the local

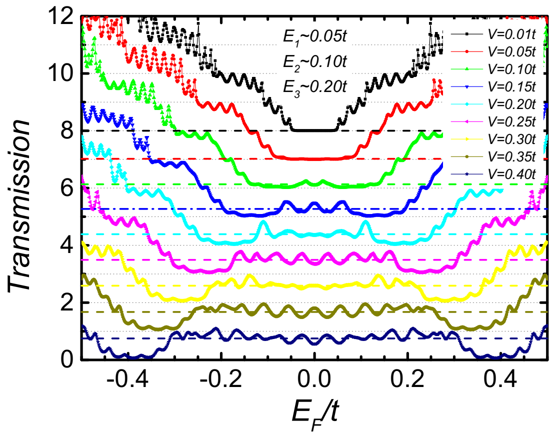

FIG. 4. Transmission as a function of the electronic energy for the pn junction shown in Fig. 3 for different potential values from $V = 0.01t$ through $V = 0.40t$. Here $M = 19$ and $U = 0$. The dashed lines correspond to $w_{\rm tun}$, Eq. (7), for each value of V. For clarity, the transmissions are shifted by $T = 1$ for successive values of V.

CNP to $+V$. Similarly, for $3L/4 < x < L$, the CNP is shifted down to $-V$. The transition from $+V$ to $-V$ happens in the region where $L/4 < x < 3L/4$. Thus, $V(\mathbf{r})$ leads to band gaps $V - E_1 < E_F < V + E_1$ and $-V - E_1 < E_F < -V + E_1$ at the "left" and "right" sides of the junction, respectively. This is illustrated by the right panel of Fig. 5. For energies around the global CNP ($E_F = 0$), that is for $-V + E_1 < E_F < V - E_1$, the available states at $x = 0$, the electrons must tunnel through at least one locally gapped region (at $x = L/2$).

The following picture emerges: For $V < E_1$ the transmission is suppressed for $|E_F| < V + E_1$ due the band gaps either at the right or at the left. (In our calculations T is small but nonzero, because we work with a finite L.) This corresponds to the cases where $V = 0.01t$ and $V = 0.05t$, shown in Fig. 4. For $V > E_1$ and $|E_F| < V - E_1$, Klein tunneling at the pn interface dominates the transmission, and the gaps appear only for increasing $|E_F|$. This transmission profile corresponds to the cases where $V > E_1$ in Fig. 4 and is qualitatively captured by the sketch presented in the right panel of Fig. 5.

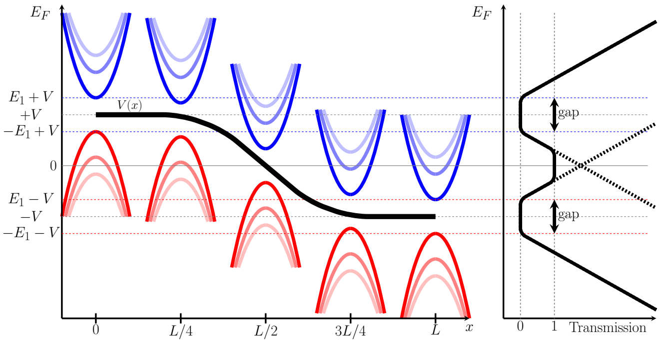

FIG. 5. Left: Sketch of the local dispersion relation at five representative points $x = 0$, $L/4$, $L/2$, $3L/4$, and L. The black line along the length L represent the potential profile $V(\mathbf{r})$ due to a smooth pn junction. The dashed gray lines at $+V$ and $-V$ indicate the local CNP for $x = 0$ and $x = L$, respectively. The blue (red) solid lines at $V + E_1$ and $V - E_1$ ($-V + E_1$ and $-V - E_1$) stand for the energies to open the first channel in the presence of the potential V at $x = 0$ ($x = L$). Right: Sketch of the transmission (solid line) as a function of E_F for the potential in the left panel. The dashed lines correspond to the undoped system transmissions, shifted up or down due to V.

Let us now estimate the magnitude of transmission at the CNP. For that purpose we adapt the semiclassical analysis of the Klein tunneling transmission presented in Ref. [14] to our case. First, we relate the local longitudinal wave number of the nth band with the electron energy E_F in the presence of a pn junction potential profile $u(x)$, as

$$E_F = v\sqrt{k_x^2(E_F,x) + (E_n/v)^2} + u(x), \tag{6}$$

where $v = \sqrt{3}ta_0/2$ and E_n is the threshold energy to open the nth channel for $u(x) = 0$. For the sake of simplicity, we approximate the pn junction potential profile to $u(x) \approx Fx$, where $F = -(2V/d)x$. At the charge neutrality point, where $E_F = 0$, the longitudinal momentum becomes $k_n(x) = v^{-1}\sqrt{F^2x^2 - E_n^2}$. In this situation, the classically forbidden region corresponds to $\ell_- < x < \ell_+$, where $\ell_\pm = \pm E_n/F$. The probability of an electron in channel n to tunnel through the classically forbidden region (gapped region) can be approximated by $w_n \approx \exp\,[i\int_{\ell_-}^{\ell_+} k(x)dx] = \exp\,(-\frac{\pi}{\sqrt{3}ta_0}\frac{dE_n^2}{V})$.

Thus, the total tunneling probability reads

$$w_{\rm tun} \approx \sum_{n=1}^{\infty} w_n = \sum_{n=1}^{\infty} \exp\left(-\frac{\pi}{2\sqrt{3}ta_0}\frac{LE_n^2}{V}\right). \tag{7}$$

Here we set $d = L/2$, since in our model the pn junction potential $u(x)$ varies from V to $-V$ in the interval $L/4 < x < 3L/4$. The contribution of each channel n to the tunneling probability in Eq. (7) decays exponentially with $E_n^2 \propto M^{-2}$. For very large M, many channels contribute to the transmission, and we can transform the sum in Eq. (7) into an integral, recovering the results of Ref. [14].

For the system studied in Fig. 4 ($L = 220\sqrt{3}a_0/4 = 234.35$ Å and $L/W = 5$), we obtain $w_{\rm tun}$ to good accuracy by summing over a small number of channels, $n \leqslant N_{\rm ch} = 3$. The ribbon band structure renders $E_1 \approx 0.05t$, $E_2 \approx 0.10t$, and $E_3 \approx 0.20t$. Around the CNP the analytical transmission $w_{\rm tun}$ (dashed lines in Fig. 4) is in nice qualitative agreement with the numerical calculated one. We attribute the small deviations to Fabry-Perot interference patterns due to the wave function mismatch at the graphene-contact interface.

These observations allow us to infer the behavior of the conductance as one increases W to realistic sample sizes: (i) the transmission for $|E_F| < V$ increases since the transverse mode energies E_n decrease with W and more transverse modes contribute to the transmission, see Eq. (7). (ii) The "satellite" gaps at $E_F = \pm V$ shrink and tend to disappear, since E_1 scales with W^{-1}. (iii) The behavior for the homopolar junctions, $|E_F| > V$, remains qualitatively the same. (iv) Finally, the magnitude of the Fabry-Perot oscillations depends on the nature of the graphene-contact interface and will be suppressed as the ratio between electron-impurity mean free path $\ell_{\rm imp}$ and the system size becomes smaller than unit, a situation that calls for an analysis along the lines of Ref. [55].

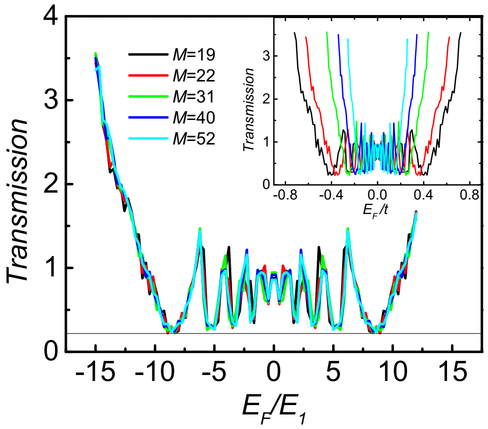

FIG. 6. Transmission as a function of the electronic energy E_F in units of E_1 for armchair edge ribbons of different widths calculated for a *pn* junction with a Gaussian profile. Inset: Same plot for energies in units of t. The solid line indicates the global transmission minimum $T_{\min}$.

B. *pn* junctions: $U \neq 0$ case

We now switch on the interaction $U = t$. The model potential is also slightly modified. We place a positive Gaussian potential centered at $(L/4, W/2)$ and a negative one at $(3L/4, W/2)$, keeping $d_y \gg W$ and $d_x = 0.24L$. This parametrization introduces a smooth variation of the *pn* junction potential close to the contacts.

Figure 6 shows the total transmission $T(E_F)$ as a function of the Fermi energy E_F for several values of M. Here, $V = 10E_1$. Since $V(\mathbf{r})$ is no longer constant either for $0 < x < L/4$ or for $3L/4 < x < L$, there is no band gap alignment in these regions, which facilitates the electronic transport. As a result, for $V - E_1 < E_F < V + E_1$ and $-V - E_1 < E_F < -V + E_1$, the transmission is nonzero, a distinction of the case analyzed in the preceding subsection. For $|E_F| < V$, the transmission $T(E_F)$ displays stronger oscillations than those of the previous case, Near the CNP, the transmission remains nearly unit.

We find that by rescaling the energy E_F as $\epsilon = E_F/E_1$, the transmission calculated for different values of M collapses into a single curve. This is illustrated in Fig. 6, inset and main panel. For $|E_F| < V$, the electron backscattering amplitude is appreciable, and its interference with the transmission process gives rise to the oscillating pattern in Fig. 6. For $|E_F| > V$ the back scattering amplitude becomes weaker and the interference effects are suppressed. Like in the $U = 0$, the main features of the transmission can be qualitatively explained by Fabry-Perot interference and Klein tunneling.

In order to understand the onset of the transmission minimum we also study (not shown here) the transmission for several ribbon widths and potential strengths $V = 5E_1$, $V = 10E_1$, $V = 15E_1$, and $V = 20E_1$. We find that: (i) V determines the energy window characterized by large interference oscillations, namely, $|E_F| < V$. (ii) The transmission has an overall nonvanishing minimum $T_{\min}$. (iii) $T_{\min}$ does not show a simple dependence on V. $T_{\min}$ increases with V until it saturates at a value close to unity, leading to a conductance of order of e^2/h. (iv) Most importantly, we conclude that deviations from a flat $V(\mathbf{r})$ close to the graphene-contact interface increase the transmission, $T_{\min} > 0$, and eliminate the energy windows of zero transmission presented in Sec. III A.

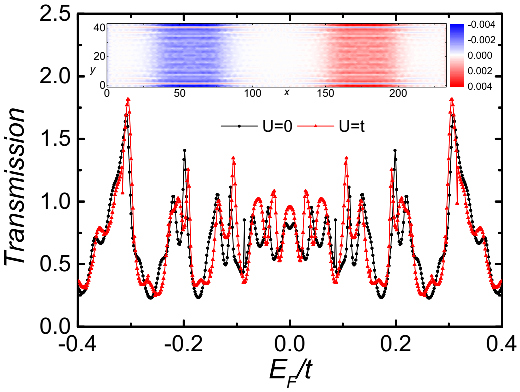

FIG. 7. Transmission as a function of E_F for $U = 0$ and $U = 1$ for an armchair edge ribbons with $M = 19$ in the vicinity of a *pn* junction with a Gaussian potential profile with $V = 0.5t$. Inset: Difference between the electronic occupancies in the noninteracting and interacting cases at $E_F = 0.0001t$.

We note that $T_{\min}$ obtained in this simple model is due to the local band energy mismatch close to the contact regions. It should not be confused with the minimum transmission in disordered graphene systems addressed in Sec. III D.

Figure 7 compares the electronic transmissions through a narrow GNR with $M = 19$ for $U = 0$ and $U = t$. The transmission in the interacting case is qualitatively similar to the noninteracting one, but there are quantitative differences, particularly close to the CNP. The interaction U corrects the local electronic density $\langle \hat{n}_{j,\sigma} \rangle$ which is also a function of the local potential V_j. Thus, the difference between the noninteracting and the interacting potentials $U\langle \hat{n}_{j,\sigma} \rangle$ becomes stronger on top of the high doped areas (see the inset of Fig. 7) and creates a new potential profile that changes the interference pattern in the transmission.

C. Focusing effects in a two Gaussian puddle geometry

Let us now study the effect of a potential variation along the transverse direction. Specifically, we analyze the transmission in a graphene ribbon with two Gaussian charge puddles. We set $d_y = 0.6Ma_0$, $d_x = 0.24L$ and place the Gaussian potentials at $(L/4, W/2)$ and $(3L/4, W/2)$. The remaining parameters are the same as in Sec. III B with $U = t$. The potential profile $V(\mathbf{r})$ is illustrated by Fig. 8 (top panel).

The middle panel of Fig. 8 shows the local transmission profile at $E_F = 0.15E_1$. Near the source (left) and the drain (right) the local transmission is almost evenly distributed across the system width. At the *pn* interface region, $x \approx L/2$, the behavior is similar. In contrast, near the center of both positive and negatively charged puddles, corresponding to the most doped regions of the system, the transmission is largely enhanced. This implies a strong suppression of the current close to the edges, due to current conservation along different ribbon cross sections.

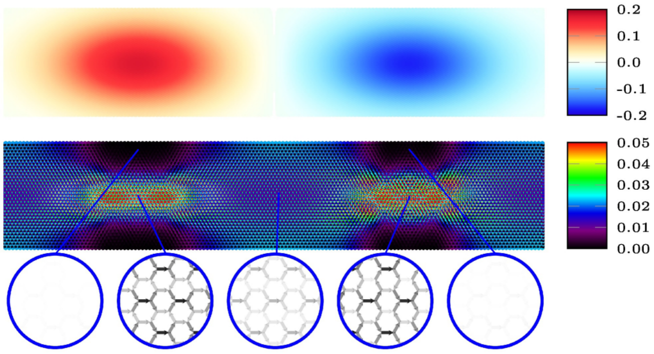

FIG. 8. Top: Potential profile $V(\mathbf{r})$ for $M = 52$. The energy scale on the right is in units of t. Middle: Corresponding local transmission at $E_F \approx 0.15E_1$. Bottom: Zoom of the local transmission at selected areas.

In summary, the Gaussian potentials not only favor the electronic propagation but also focus the transmission on the highly doped areas. This effect can be interpreted in terms of the picture discussed in the previous section. Close to the center of the puddles, the potential $V(\mathbf{r})$ shifts the local dispersion relation. "Local" transmission modes are opened if $|V(\mathbf{r}_c)| > E_n^*$. Note that here the threshold energies E_n^* are related to the puddle width a, rather then to the system width W.

As in the previous case, we find that the transmissions $T(E_F)$ for different widths W collapse very nicely to a single curve by scaling $\epsilon = E_F/E_1$, particularly for the energy window where $|\epsilon| < 5$, see Fig. 9. We expect a similar result if we scale E_F by E_1^*, since in our model the ratio between the puddle size a and the system width W does not change with M. These observations suggest that by proper scaling one can address systems with realistic sizes.

Upon first inspection, the transmissions $T(E_F)$ shown in Figs. 6 and 9 look similar. A more detailed analysis indicates that in the present case: (i) The value of the transmission minimum is smaller. (ii) The interference pattern covers a smaller energy window. We speculate that those results are due to the smaller doping of the areas near the edges. The ribbon accommodates a smaller number of propagating states, compared to the pn junction case, so that the total transmission through a ribbon cross section is smaller. Since the total doping of the ribbon is smaller, the effective scattering potential that determines the energy window of the interference pattern is also smaller.

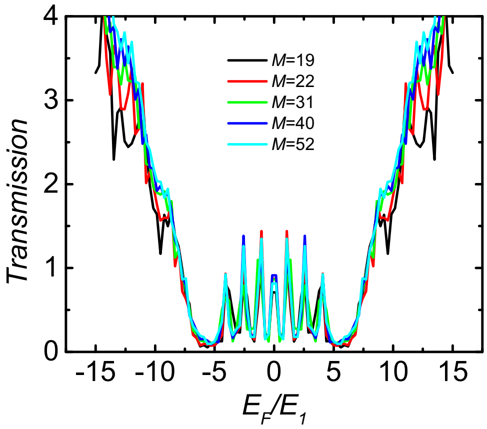

FIG. 9. Transmission as a function of the electronic energy E_F in units of E_1 for armchair edge graphene ribbons of different widths M.

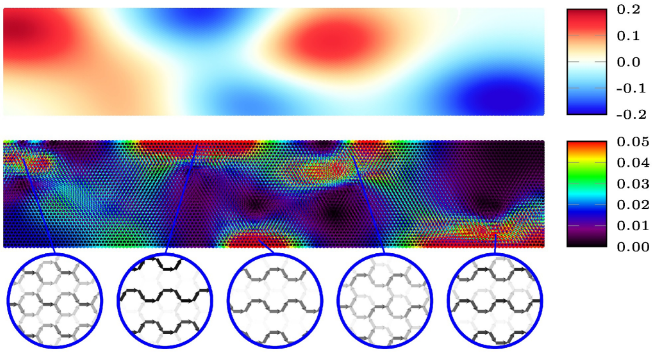

FIG. 10. Top: Random potential profile $V(\mathbf{r})$ realization (see text for details). The energy scale in the right is in units of t. Middle: Corresponding dimensionless local current density at energy $E_F \approx 2.31E_1 = 0.04t$. Bottom: Zoom of selected areas showing the local transmission in details.

D. Disordered charge puddles

In this subsection we study the case of randomly distributed charge puddles that are ubiquitous in graphene samples [1,16,17,19,20]. We analyze two limiting cases, namely, small and large charge puddles, as compared with W. The corresponding $V(\mathbf{r})$ are shown in the top panels of Figs. 10 (small puddles) and 11 (large puddles). The random potential is generated according to Eq. (2) with $N_G = 8$, $d_x = 62a_0$, and $d_y = 31a_0$ for a system with dimensions $M = 52$ ($W = 12.5$ nm) and $N = 604$ ($L = 62.8$ nm). In both cases we set $V = 0.2t = 11.44E_1$.

The middle and bottom panels of Figs. 10 and 11 show that, as in the previous subsection, the local transmission is focused on the maximally n and p doped areas. The "large" puddles illustrated in Fig. 11 induce higher local currents than the "small" ones corresponding to Fig. 10 (see scales).

The results indicate that the local transmission depends strongly on the potential landscape, since the number of propagating modes increases with both puddle size a and

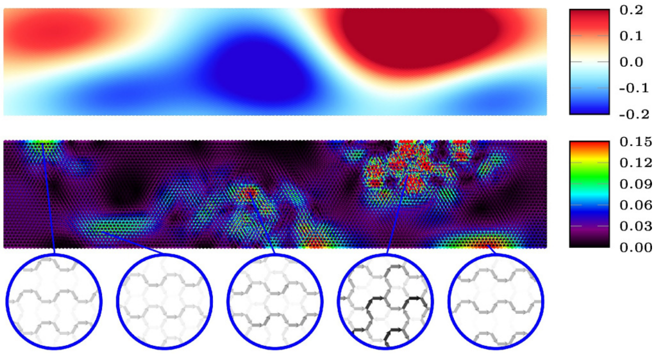

FIG. 11. Same as in Fig. 10 for a different random potential realization.

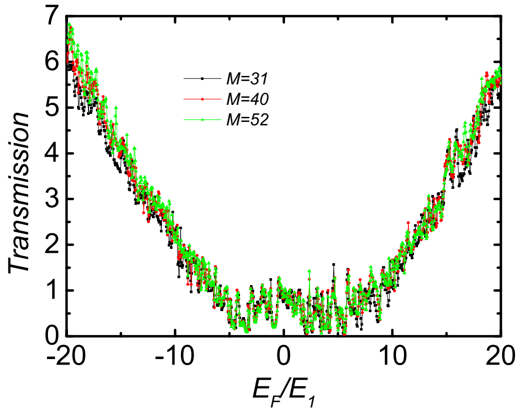

FIG. 12. Transmission as a function of the electronic energy in units of E_1. We show the results for $M = 52$ with the potential profile in Fig. 10 and for $M = 31,40$ using a similar potential profile scaled down to smaller sizes keeping the aspect ratio.

local doping $\delta n(\mathbf{r}) \equiv n(\mathbf{r}, V \neq 0) - n(\mathbf{r}, V = 0)$. In the limit of $a(\delta n)^{1/2} \gg 1$, the random resistor model put forward in Ref. [18] estimates the conductivity at the CNP to be $\sigma_{\min} \approx (e^2/\hbar)(a^2\delta n)^{0.41}$, where a and δn are defined by the correlation function $\langle \delta n(\mathbf{r})\delta n(\mathbf{r}')\rangle \equiv \delta n^2 F(|\mathbf{r} - \mathbf{r}'|/a)$ [18]. The model is semiclassical and does not include interference effects. Despite these limitations, $\sigma_{\min}$ is in qualitative agreement with our numerical findings which we discuss next, namely, that the transmission near the CNP is larger for the "large" charge puddle case than for the "small" puddle one.

Figures 12 and 13 show the total transmission corresponding to the potential profiles presented by Figs. 10 and 11, respectively. Here, by expressing the energy as $\epsilon = E_F/E_1$, the transmissions for different system sizes no longer collapse into a single curve. Nonetheless, in all studied cases $T(\epsilon)$ shows a similar average behavior and fluctuations reminiscent of the universal conductance fluctuations (UCF) ubiquitous in disordered mesoscopic systems.

Around the CNP ($|E/E_1| \lesssim 10$) the number of open modes depends strongly on the typical puddle size: The larger the puddles the smaller E_n^*. Hence, one expects to observe an enhanced transmission for the "large" puddle case. Away from the CNP ($|E_F/E_1| \gtrsim 10$), Figs. 12 and 13 show that the transmission for the "large" puddles case is smaller than that for the "small" ones. We interpret this feature as follows: Here the number of open modes is dictated by E_F. Stronger disorder potential fluctuations are more effective to mix different modes and to favor backscattering, giving rise to a smaller transmission. Thus, disordered puddles are detrimental to the transport as one approaches the semiclassical regime, but they enhance the transmission minimum around the CNP. We note that here the transmission minimum survives even in the absence of evanescent modes [6].

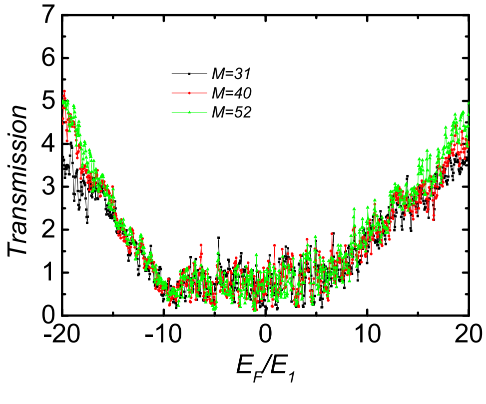

FIG. 13. Same as in Fig. 12 using the potential profile in Fig. 11.

We also compare the transmission for $U = 0$ and $U = t$. The results are qualitatively similar. Our calculations (not shown here) indicate that the Hubbard mean field interaction corrects for an overestimation of the onsite electronic density but has little impact on the local or total transmissions through the systems. The simple interference patterns we observe in the single pn junction are quenched by the random potential. The latter leads to UCF that makes it difficult to sort out the small differences between the interacting and noninteracting transmissions.

We make connections with experiments by estimating the typical values of E_1^* for realistic size samples. We find that graphene charge puddles with sizes $a \approx 20\ldots50$ nm correspond to $E_1^* \approx 10\ldots30$ meV. Typical graphene on silicon oxide samples [20] show $\delta V/E_1^* > 1$. Hence, charge puddle disorder enhances the conductivity and guarantees a nonvanishing conductivity minimum at the CNP, independent of the contribution due to evanescent modes. For graphene on hBN, where $\delta V \approx 5$ meV [20], only a small fraction of puddles meet the criterion $V_{\rm loc}(\mathbf{r})/E_1^* \gtrsim 1$. In this situation, charge puddle fluctuation assisted transport is very unfavorable. Hence, for graphene flakes on hBN with aspect ratios $L/W > 3$, where evanescent modes contribute very little to the transmission, one expects the conductivity at the CNP to be strongly suppressed. We believe that this scenario is consistent with the experimental report [30] of an insulator behavior of single-layer graphene on hBN at the neutrality point.

IV. CONCLUSIONS

We studied the effect of charge puddles in the transmission minimum of single layer graphene stripes by means of a microscopic model based on a spin resolved tight-binding Hamiltonian including electron-electron interactions via a Hubbard mean field term. To understand the conductivity at the CNP and scale up our results to experimental size samples, we used the recursive Green's function technique to obtain the transmission through semiconductor graphene strips with an armchair edge. The charge puddles are modeled by a local Gaussian disordered potential.

First we studied pristine graphene systems with a smooth pn junction. This simple model shows that the onset of the transmission minimum at the CNP occurs for potential strengths V larger than the threshold energy E_1 to open the first conducting transverse mode of the system. The transmission near the CNP is robust against smooth changes in the potential along the propagation direction, and it does not depend much on whether the doping is n- or p-type. We showed that all transmission features around the CNP can be explained by Klein tunneling and by Fabry-Perot interference due to the mismatch of the wave functions at the graphene-contacts interface.

Next, we studied the transmission through a system with two charge puddles separated by a smooth *pn* interface. In this setting, we find that the overall total transmission decreases and the local transmission is focused around the maximally *p*- or *n*-doped regions, corresponding to the centers of the puddles. We showed that the electron-electron interaction U corrects the electronic density giving rise to an interference pattern in the electronic transmission that differs quantitatively from the noninteracting case around the CNP but that does not qualitatively change the transmission. We demonstrated that by using E_1 (or E_1^*, see text) as the energy unit, the transport properties around the CNP become independent of the system size. This powerful result allows us to address realistic sized systems by scaling up our model calculations obtained for small systems, whose sizes are imposed by computational limitations.

Finally, we also modeled disordered charge puddle distributions showing that, depending on the puddles sizes, there is a nonvanishing average transmission minimum around the CNP with fluctuations similar to UCF. The numerical results can be qualitatively explained by Klein tunneling at the *pn* interfaces formed at the puddles interface and the enhanced (focused) local transmission at the maximally doped areas. In this case, we find that the interaction U does not appreciably affect the electronic transmission.

Our results show that, for graphene on silicon oxide, the local chemical fluctuations [20,28] are sufficiently large to explain a nonvanishing conductivity minimum at the charge neutrality point $\sigma_{\rm CNP}$ in terms of charge puddle disorder-assisted transport. On the other hand, in typical graphene samples on hBN [20], only a small fraction of puddles show $V_{\rm loc}(\mathbf{r})/E_1^* \gtrsim 1$. In this case, unless compensated by contributions from evanescent modes, one expects a strong suppression of $\sigma_{\rm CNP}$. This scenario is consistent with the recent experimental report [30] of an insulator behavior of $\sigma_{\rm CNP}$ in graphene on hBN samples with an aspect ratio $L/W \gtrsim 3$.

In summary, this study separates the contribution of evanescent modes from that of charge puddles in the transport properties of graphene strips close to the CNP. We found that the presence of electron and hole puddles in graphene enhances the electronic transmission at the CNP depending on their size and charge, represented in our model by a and V. We argue that our findings provide a scenario to explain transport experiments in graphene deposited on both $\mathrm{SiO_2}$ [7,8] and hBN substrates [30].

ACKNOWLEDGMENT

This work is supported by the Brazilian funding agencies CAPES, CNPq, and FAPERJ.

[1] A. H. Castro Neto, F. Guinea, N. M. R. Peres, K. S. Novoselov, and A. K. Geim, Rev. Mod. Phys. **81**, 109 (2009).
[2] E. R. Mucciolo and C. H. Lewenkopf, J. Phys.: Condens. Matter **22**, 273201 (2010).
[3] S. Das Sarma, S. Adam, E. H. Hwang, and E. Rossi, Rev. Mod. Phys. **83**, 407 (2011).
[4] F. Miao, S. Wijeratne, Y. Zhang, U. C. Coskun, W. Bao, and C. N. Lau, Science **317**, 1530 (2007).
[5] R. Danneau, F. Wu, M. F. Craciun, S. Russo, M. Y. Tomi, J. Salmilehto, A. F. Morpurgo, and P. J. Hakonen, Phys. Rev. Lett. **100**, 196802 (2008).
[6] J. Tworzydlo, B. Trauzettel, M. Titov, A. Rycerz, and C. W. J. Beenakker, Phys. Rev. Lett. **96**, 246802 (2006).
[7] A. K. Geim and K. S. Novoselov, Nat. Mater. **6**, 183 (2007).
[8] Y.-W. Tan, Y. Zhang, K. Bolotin, Y. Zhao, S. Adam, E. H. Hwang, S. Das Sarma, H. L. Stormer, and P. Kim, Phys. Rev. Lett. **99**, 246803 (2007).
[9] A. Rycerz, J. Tworzydlo, and C. W. J. Beenakker, Europhys. Lett. **79**, 57003 (2007).
[10] M. Titov, Europhys. Lett. **79**, 17004 (2007).
[11] C. H. Lewenkopf, E. R. Mucciolo, and A. H. Castro Neto, Phys. Rev. B **77**, 081410(R) (2008).
[12] P.-L. Zhao, S. Yuan, M. I. Katsnelson, and H. De Raedt, Phys. Rev. B **92**, 045437 (2015).
[13] M. I. Katsnelson, K. S. Novoselov, and A. K. Geim, Nat. Phys. **2**, 620 (2006).
[14] V. V. Cheianov and V. I. Fal'ko, Phys. Rev. B **74**, 041403 (2006).
[15] S. Hikami, A. I. Larkin, and Y. Nagaoka, Prog. Theor. Phys. **63**, 707 (1980).
[16] J. Martin, N. Akerman, G. Ulbricht, T. Lohmann, J. H. Smet, K. v. Klitzing, and A. Yacoby, Nat. Phys. **4**, 144 (2008).
[17] Y. Zhang, V. W. Brar, C. Girit, A. Zettl, and M. F. Crommie, Nat. Phys. **5**, 722 (2009).
[18] V. V. Cheianov, V. I. Fal'ko, B. L. Altshuler, and I. L. Aleiner, Phys. Rev. Lett. **99**, 176801 (2007).
[19] M. I. Katsnelson, *Graphene: Carbon in Two Dimensions* (Cambridge University Press, Cambridge, 2012).
[20] J. Xue, J. Sanchez-Yamagishi, D. Bulmash, P. Jacquod, A. Deshpande, K. Watanabe, T. Taniguchi, P. Jarillo-Herrero, and B. J. LeRoy, Nat. Mater. **10**, 282 (2011).
[21] L. A. Ponomarenko, R. Yang, T. M. Mohiuddin, M. I. Katsnelson, K. S. Novoselov, S. V. Morozov, A. A. Zhukov, F. Schedin, E. W. Hill, and A. K. Geim, Phys. Rev. Lett. **102**, 206603 (2009).
[22] N. J. G. Couto, B. Sacépé, and A. F. Morpurgo, Phys. Rev. Lett. **107**, 225501 (2011).
[23] A. Deshpande, W. Bao, F. Miao, C. N. Lau, and B. J. LeRoy, Phys. Rev. B **79**, 205411 (2009).
[24] M. Gibertini, A. Tomadin, F. Guinea, M. I. Katsnelson, and M. Polini, Phys. Rev. B **85**, 201405 (2012).
[25] S. C. Martin, S. Samaddar, B. Sacépé, A. Kimouche, J. Coraux, F. Fuchs, B. Grévin, H. Courtois, and C. B. Winkelmann, Phys. Rev. B **91**, 041406 (2015).
[26] E. Rossi and S. Das Sarma, Phys. Rev. Lett. **101**, 166803 (2008).
[27] C. R. Dean, A. F. Young, I. Meric, C. Lee, L. Wang, S. Sorgenfrei, K. Watanabe, T. Taniguchi, P. Kim, K. L. Shepard, and J. Hone, Nat. Nanotechnol. **5**, 722 (2010).
[28] A. Deshpande, W. Bao, Z. Zhao, C. N. Lau, and B. J. LeRoy, Phys. Rev. B **83**, 155409 (2011).
[29] S. Adam, P. W. Brouwer, and S. Das Sarma, Phys. Rev. B **79**, 201404 (2009).

[30] F. Amet, J. R. Williams, K. Watanabe, T. Taniguchi, and D. Goldhaber-Gordon, Phys. Rev. Lett. **110**, 216601 (2013).
[31] C. R. Woods, L. Britnell, A. Eckmann, R. S. Ma, J. C. Lu, H. M. Guo, X. Lin, G. L. Yu, Y. Cao, and R. V. Gorbachev, Nat. Phys. **10**, 451 (2014).
[32] L. A. Ponomarenko, A. K. Geim, A. A. Zhukov, R. Jalil, S. V. Morozov, K. S. Novoselov, I. V. Grigorieva, E. H. Hill, V. V. Cheianov, V. I. Fal'ko, K. Watanabe, T. Taniguchi, and R. V. Gorbachev, Nat. Phys. **7**, 958 (2011).
[33] D. A. Areshkin and B. K. Nikolić, Phys. Rev. B **79**, 205430 (2009).
[34] C. H. Lewenkopf and E. R. Mucciolo, J. Comput. Electron. **12**, 203 (2013).
[35] J. Fernández-Rossier, J. J. Palacios, and L. Brey, Phys. Rev. B **75**, 205441 (2007).
[36] Y.-W. Son, M. L. Cohen, and S. G. Louie, Phys. Rev. Lett. **97**, 216803 (2006).
[37] L. Brey and H. A. Fertig, Phys. Rev. B **73**, 235411 (2006).
[38] We estimate that $E_1 \approx a_0 t/W$ from the analysis of E_1 versus W^{-1} obtained from the numerical solution of the tight-binding model for several semiconductor pristine armchair-edge graphene strips of widths up to $W = 160a_0$ (a similar analysis to that in Ref. [37]).
[39] M. Y. Han, B. Özyilmaz, Y. Zhang, and P. Kim, Phys. Rev. Lett. **98**, 206805 (2007).
[40] E. R. Mucciolo, A. H. Castro Neto, and C. H. Lewenkopf, Phys. Rev. B **79**, 075407 (2009).
[41] Y. Meir and N. S. Wingreen, Phys. Rev. Lett. **68**, 2512 (1992).
[42] H. Haug and A. J. Jauho, *Quantum Kinetics in Transport and Optics of Semiconductors*, Solid-State Sciences, Vol. 123 (Springer, Berlin, Heidelberg, 2008).
[43] T. Ozaki, Phys. Rev. B **75**, 035123 (2007).
[44] A. Croy and U. Saalmann, Phys. Rev. B **80**, 073102 (2009).
[45] D. A. Areshkin and B. K. Nikolić, Phys. Rev. B **81**, 155450 (2010).
[46] D. Singh, H. Krakauer, and C. S. Wang, Phys. Rev. B **34**, 8391 (1986).
[47] S. Ihnatsenka, I. V. Zozoulenko, and M. Willander, Phys. Rev. B **75**, 235307 (2007).
[48] When calculating the electronic properties as a function of μ, the number of iterations can be further diminished by using as the initial guess for $\mu + \Delta\mu$ the converged electronic density obtained for μ. In this case, one has to find an optimal compromise between the number of self-consistent iterations and the chemical potential steps $\Delta\mu$.
[49] S. Nonoyama and A. Oguri, Phys. Rev. B **57**, 8797 (1998).
[50] A. Cresti, R. Farchioni, G. Grosso, and G. P. Parravicini, Phys. Rev. B **68**, 075306 (2003).
[51] B. K. Nikolić, L. P. Zârbo, and S. Souma, Phys. Rev. B **73**, 075303 (2006).
[52] L. P. Zârbo and B. K. Nikolić, Europhys. Lett. **80**, 47001 (2007).
[53] M. Schüler, M. Rösner, T. O. Wehling, A. I. Lichtenstein, and M. I. Katsnelson, Phys. Rev. Lett. **111**, 036601 (2013).
[54] A. R. Carvalho, J. H. Warnes, and C. H. Lewenkopf, Phys. Rev. B **89**, 245444 (2014).
[55] M. M. Fogler, L. I. Glazman, D. S. Novikov, and B. I. Shklovskii, Phys. Rev. B **77**, 075420 (2008).